CHALMERS
UNIVERSITY OF TECHNOLOGY

Angled Flip-Chip Integration of VCSELs on Silicon Photonic Integrated Circuits

Angled Flip-Chip Integration of VCSELs on Silicon Photonic Integrated Circuits

Mehdi Jahed[1,*], Alexander Caut[1,*], Jeroen Goyvaerts[2,*], Marc Rensing[3],
Magnus Karlsson[1], *Fellow Optica, Senior Member IEEE*, Anders Larsson[1], *Fellow Optica, Fellow IEEE*,
Günther Roelkens[2], Roel Baets[2], *Fellow Optica, Fellow IEEE* and Peter O'Brien[3]
1) Photonics Laboratory, Department of Microtechnology and Nanoscience, Chalmers University of Technology, SE-412 96 Göteborg, Sweden
2) Photonics Research Group, Ghent University-imec, Technologiepark-Zwijnaarde 126, 9052 Ghent, Belgium
3) Tyndall National Institute, Lee Maltings Complex, Cork, Ireland
*) Contributed equally

***Abstract*—An investigation of angled flip-chip integration of a singlemode 850 nm vertical-cavity surface-emitting laser (VCSEL) on a silicon nitride photonic integrated circuit (PIC) is presented. Using numerical FDTD simulations, we consider the conditions under which the VCSEL can be integrated at an angle over a grating coupler with high coupling efficiency and low optical feedback. With both coupling efficiency and feedback decreasing with increasing angle, there is a trade-off. With co-directional coupling, first-order diffraction loss sets in at a critical angle, which further reduces the coupling efficiency. No such critical angle exists for contra-directional coupling. We also experimentally demonstrate angled flip-chip integration of GaAs-based 850 nm single transverse and polarization mode VCSELs over grating couplers on a silicon-nitride PIC. At the output grating coupler, light is either collected by an optical fiber or converted to a photocurrent using a flip-chip integrated GaAs-based photodetector. The latter forms an on-PIC optical link. We measured an insertion loss of 21.9, 17.6 and 20.1 dB with a singlemode fiber, multimode fiber and photodetector over the output grating coupler, respectively.**

***Index Terms*—Flip-chip integration, vertical-cavity surface-emitting laser, silicon-nitride photonic integrated circuit, coupling efficiency, optical feedback**

I. Introduction

Light source integration on silicon photonic integrated circuits (PICs) can be achieved by hybrid and heterogeneous integration [1]. This includes a variety of pick-and-place techniques such as flip-chip integration [2], transfer printing [3], butt- or edge-coupling [4] and micro-optical-bench (MOB) integration [5], or a combination of these methods. Flip-chip integration creates a mechanical and electrical bond between the light source and the PIC by soldering. Transfer printing involves pick-up of pre-processed device coupons from a source wafer and subsequent printing on the host PIC wafer using a stamp. For butt-coupling, the light source is aligned to a waveguide facet of the PIC. The MOB contains not only the light source but also micro-optical elements for beam collimation and redirection. For both flip-chip integration, transfer printing and MOB integration, a grating coupler (GC) on the PIC is used for grating-assisted coupling to the PIC waveguide [6].

Potential applications of silicon PICs with an integrated light source include datacom transceivers and a variety of PIC-based sensors. For instance, with multiple high-speed vertical-cavity surface-emitting lasers (VCSELs) at different wavelengths flip-chip integrated on a silicon PIC for multiplexing and fiber coupling, a compact and energy efficient transmitter module for high-capacity wavelength-multiplexed optical interconnects can be built [7]. An example of a PIC-based sensor is the integrated optical gas sensor based on absorption spectroscopy for e.g. highly sensitive measurements of gas concentrations, where the spectral region of interest is interrogated by an integrated tunable light laser [8].

Flip-chip integration of a VCSEL over a GC [2], [9], [10], [11] is of interest because the VCSEL consumes less power and has a smaller footprint than most other light sources. With flip-chip integration, the performance of the VCSEL can be independently optimized and tailored for the specific requirements set by the PIC and the application. For high coupling efficiency to the singlemode Si or Si_3N_4 waveguide, the VCSEL must be singlemode (SM) and its linear polarization must be stable and properly aligned to the grating lines. However, with SM-VCSELs being sensitive to optical feedback [12], optical back-reflection to the VCSEL must also be avoided. In addition, most applications require uni-directional coupling to the waveguide. Both requirements can be met by flip-chip integration at an angle with respect to the surface of the GC (Fig. 1) [2].

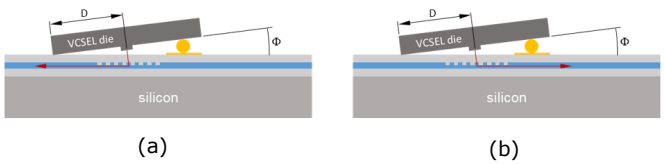

Fig. 1. Angled flip-chip integration of a VCSEL over a GC. Two coupling geometries are shown, (a) contra-directional coupling, and (b) co-directional coupling. A variation of flip-chip angle Φ leads to a variation of the incidence angle of the beam from the VCSEL on the GC while variations of both angle Φ and distance D lead to a variation of the VCSEL-to-GC distance.

For a given length D from the VCSEL to the edge of the

VCSEL die (Fig. 1), a certain minimum angle Φ is required to suppress optical feedback to the VCSEL from specular reflection (0:th order diffraction) at the GC. However, when the angle exceeds a critical angle Φ_c, first order diffraction into the cladding layers of the waveguide may occur, which reduces the coupling efficiency. This depends on whether the coupling is co- or contra-directional. With the VCSEL and the bond pads lithographically defined and aligned to the edge of the VCSEL die that touches the PIC, the only die dimension of relevance for Φ_c is D.

Here we investigate how both coupling efficiency and optical feedback depend on length D and angle Φ and examine the trade-offs using numerical FDTD simulations. We also demonstrate angled flip-chip integration of single transverse and polarization mode 850 nm VCSELs [13] over GCs on silicon-nitride (SiN) PICs, with light at the output GC either collected by an optical fiber or converted to a photocurrent by a flip-chip integrated photodetector (PD).

In Sections 2 and 3, we use a most simple Si_3N_4/SiO_2 GC on a Si substrate to study general trends, dependencies and trade-offs for coupling efficiency and optical feedback. In Section 4, we present results from experiments where a more advanced, higher efficiency GC design was used. A summary with conclusions is provided in Section 5.

II. Diffraction orders and coupling efficiency

First order grating diffraction is used to couple the light incident from the VCSEL to the waveguide [6]. However, under certain conditions, first order diffraction may also generate diffraction components that radiate into the cladding layers. When this occurs, the coupling efficiency to the waveguide is reduced.

We consider the generic GC design shown in Fig. 2. From considerations of phase matching (Bragg condition), the grating period Λ is given by:

$$\Lambda = \frac{\lambda_0}{n_{\text{eff}} \pm \sin\Phi}, \tag{1}$$

where the minus (plus) sign applies to the co- (contra-) directional coupling. Here, λ_0 is the free space wavelength, n_{eff} is the effective mode index of the waveguide and Φ is the angle of incidence.

We first study the case of contra-directional coupling (Fig. 3). With the grating period Λ being smaller than the wavelength in the waveguide (λ_0/n_{eff}), first order diffraction into the cladding layers cannot occur for any grating period or corresponding input angle Θ. There is therefore no limit to the incident angle with respect to additional diffraction loss and the angle can be sufficiently large to avoid optical feedback to the VCSEL.

We next consider the case of co-directional coupling (Fig. 4). With the grating period Λ being larger than the wavelength in the waveguide, there is a critical grating period Λ_c and

corresponding critical angle of incidence Θ_c beyond which first order diffraction into the cladding layers occurs (Fig. 4b):

$$\Lambda_c = \frac{2\lambda_0}{n_{\text{eff}} + n_1}, \tag{2}$$

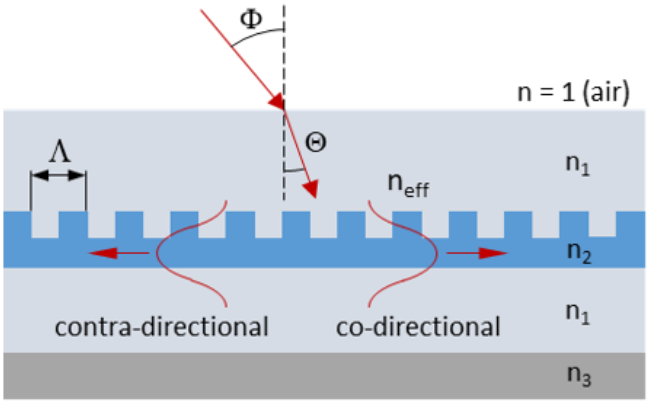

Fig. 2. Generic grating coupler with refractive indices, grating period, and angles of incidence defined, used for identifying diffraction orders for co- and contra-directional coupling and their dependence on incident angle.

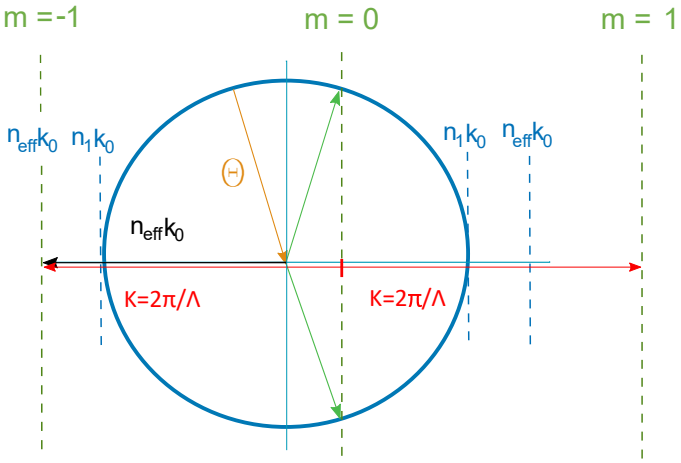

Fig. 3. Wavevector diagram for contra-directional coupling where $\Lambda < \lambda_0/n_{\text{eff}}$. Diffraction orders are denoted by m. The grating vector is K and the refractive index of the cladding layers (assumed the same) is n_1. With decreasing grating period Λ, and therefore increasing in-coupling angle Θ, there is no onset of first order diffraction into the cladding layers. $k_0 = 2\pi/\lambda_0$.

$$\Theta_c = \arcsin\left(\frac{n_{\text{eff}} - n_1}{2n_1}\right), \tag{3}$$

where n_1 is the refractive index of the cladding layers (assumed the same).

To find the corresponding critical angle of incidence from the VCSEL, Φ_c (angle of flip-chip integration), we account for refraction at the PIC surface (Fig. 2):

$$\Phi_c = \arcsin(n_1 \sin\Theta_c), \tag{4}$$

This implies that, for co-directional coupling and depending on the waveguide and grating parameters, the critical angle may not be large enough to suppress optical feedback while avoiding additional coupling loss due to first order diffraction into the cladding layers.

For a more thorough and quantitative analysis of coupling efficiency and its dependence on VCSEL and flip-chip parameters and coupling direction, the coupling efficiency was

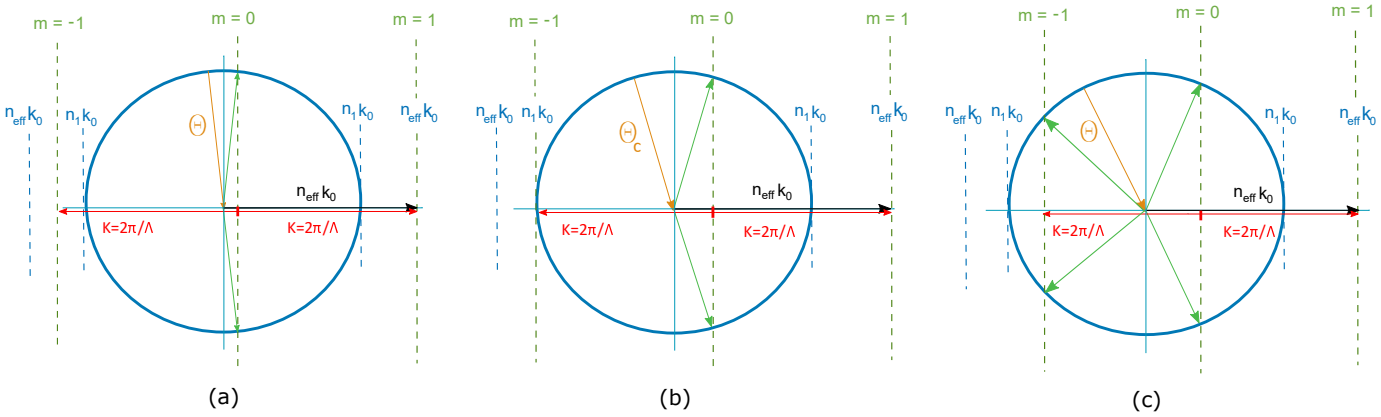

Fig. 4. Wavevector diagram for co-directional coupling where $\Lambda > \lambda_0/n_{\text{eff}}$. Diffraction orders are denoted by m. The grating vector is K and the refractive index of the cladding layers (assumed the same) is n_1. With increasing grating period Λ, (a) to (c), and therefore increasing in-coupling angle Θ, there is an onset of first order diffraction into the cladding layers at a critical angle Θ_c. $k_0 = 2\pi/\lambda_0$.

simulated for different angles Φ and lengths D for both co- and contra-directional coupling. Different combinations of Φ and D result in different distances from the VCSEL to the GC. The simulations were carried out using Lumerical 2D FDTD [14] for a uniform GC with constant period, straight gratings lines, a length of 17 µm along the coupling direction and a width of 10 µm perpendicular to the coupling direction (For the 3D simulations in section 3 we chose a grating width of 10 µm, which contains 97.5% of the total VCSEL beam power in the case D = 145 µm and Φ = 11°). The grating is a 50% duty cycle grating etched to a depth of 150 nm in a 300 nm thick Si_3N_4 core layer, sandwiched between a 3.3 µm thick lower SiO_2 cladding layer and a 2.0 µm thick upper SiO_2 cladding layer. The waveguide layers are on top of a Si substrate which is strongly absorbing at the wavelength considered (850 nm). The refractive indices of Si_3N_4, SiO_2 and Si at 850 nm were set to 1.90, 1.455, and 3.65, respectively. The VCSEL is SM with an emission wavelength of 850 nm and generates a Gaussian beam with a $1/e^2$ waist diameter of 3.8 µm at the VCSEL surface and a full $1/e^2$ divergence angle of 16° [13]. The light from the VCSEL is polarized along the grating lines. The GC couples the light from the VCSEL to the TE-polarized mode of the waveguide.

For each angle Φ and each coupling direction, the angle was swept around the values given by Eq. (1) to find the optimal grating period for maximum coupling efficiency using 2D FDTD. Fig. 5 shows the optimal grating periods for angles between 8° and 15° for both co- and contra-directional coupling. The optimal periods from the FDTD simulations are reasonably close to those given by Eq. (1) with the effective mode index calculated as the average between the mode indices in the etched and unetched parts of the 50% duty cycle grating.

Following the identification of optimal grating period for every angle, the coupling efficiency was calculated using 2D FDTD for different lengths D (from 100 to 200 µm, in steps of 10 µm) and angles Φ (from 8° to 15°, in steps of 1°). This yields a distance from the VCSEL to the GC from 14 to 54 µm. The lateral position of the VCSEL was for each case adjusted to have the light spot at the optimum position on the

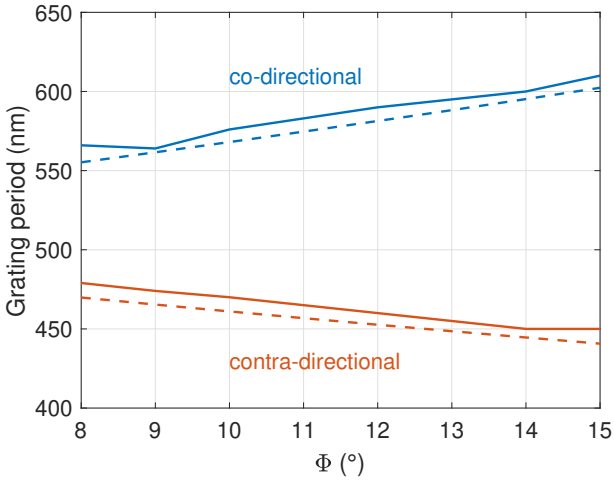

Fig. 5. Grating period for highest coupling efficiency vs. angle for co-directional (blue) and contra-directional (orange) coupling. The dashed curves represent periods calculated using Eq. 1. The solid curves represent periods from the 2D FDTD simulations.

GC for highest coupling efficiency. A monitor was placed in the waveguide, 3 µm from the GC, to monitor the power in the waveguide. The calculated coupling efficiency as a function of D and Φ for contra- and co-directional coupling is shown in Fig. 6a and b, respectively.

The simulations show that there is a critical angle for co-directional coupling (around 13°) at which the coupling efficiency suddenly drops by about 1 dB for all values of D (Fig. 6b). This is due to the onset of first order diffraction into the cladding layers, which was confirmed by placing a monitor in the lower cladding layer (Fig. 7). At D = 150 µm, with contra-directional coupling, the coupling efficiency is > -6.3 dB up to an angle of 14°. With co-directional coupling, the coupling efficiency is generally lower. The dependence of coupling efficiency on length D and angle Φ in Fig. 6 shows a relatively strong dependence on Φ and a weaker dependence on D, for both the co- and contra-directional case.

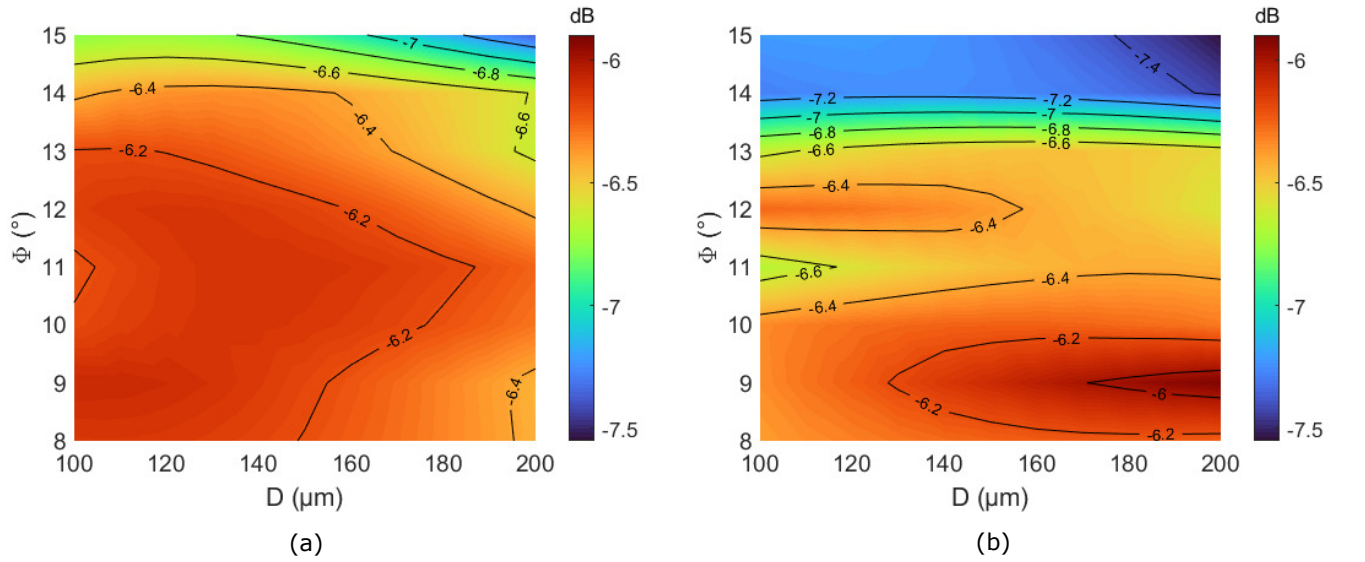

Fig. 6. Results from 2D FDTD simulations for the coupling efficiency at different lengths D and angles Φ with optimal grating periods for contra-directional (a) and co-directional (b) coupling.

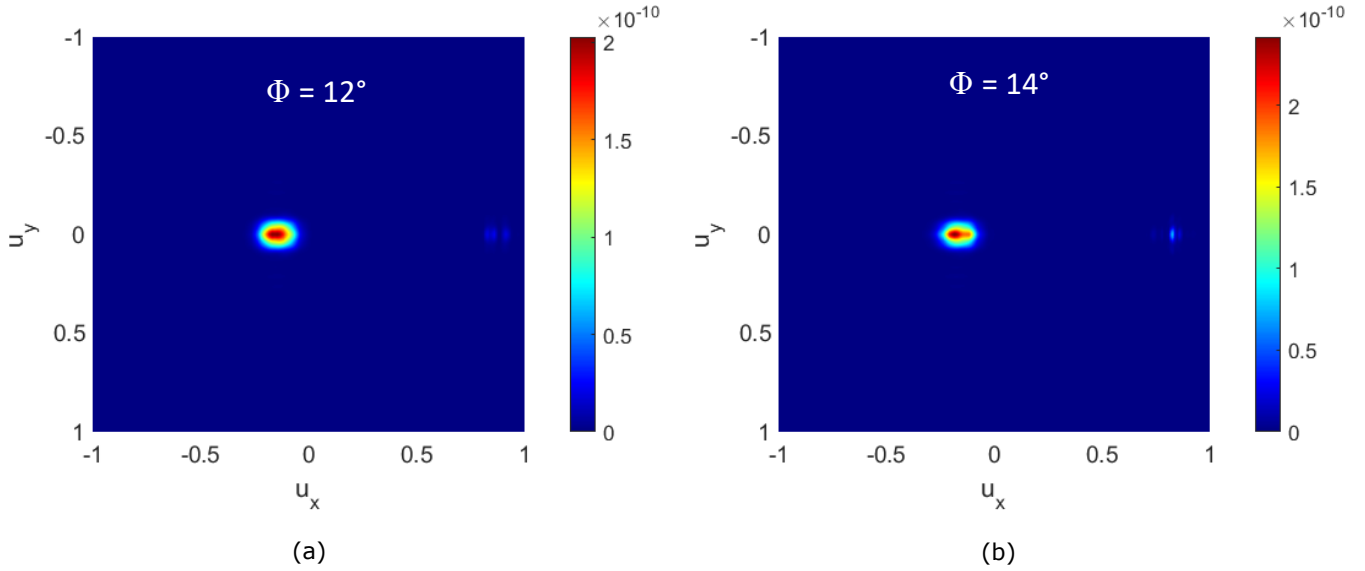

Fig. 7. Diffraction into the lower cladding layer for D = 150 μm and Φ = 12° (a) and 14° (b) with co-directional coupling. The bright spot at u_x = ~ −0.1 is due to 0:th order transmission through the GC. The faint spot appearing at u_x = ~ 0.8 for 14° incident angle is caused by first order diffraction. This is not observed for an incident angle of 12° (below the critical angle), nor for any angle with contra-directional coupling.

III. Optical Feedback

Optical feedback to the VCSEL is caused by specular reflection (0:th order diffraction) at the GC (Fig. 8). The feedback should be sufficiently low, below -30 dB [12], to avoid feedback-induced instabilities in the SM-VCSEL. We have therefore also conducted a careful analysis of feedback using FDTD for different values of D and Φ.

Optical feedback is calculated as the integral overlap of the VCSEL near-field and the reflected light on the VCSEL surface [15]:

$$\eta = \frac{|\int E_{RF} E_{NF}^{*} dA|^2}{\int |E_{RF}|^2 dA \int |E_{NF}|^2 dA} \quad (5)$$

where E_{RF} is the electrical field of the reflected light, E_{NF} is the electrical field of the VCSEL near-field and dA is the differential area element over which the integration is performed. Since this requires 3D simulations, which are heavy and time consuming, most of the simulations were carried out in 2D. In this case, optical feedback is calculated by integration along the coupling direction (x-direction, Fig. 8), according to:

$$\eta = \frac{|\int E_{RF}(x) E_{NF}^{*}(x) dx|^2}{\int |E_{RF}(x)|^2 dx \int |E_{NF}(x)|^2 dx} \quad (6)$$

The level of optical feedback depends on the incident angle Φ and the length D from the VCSEL to the edge

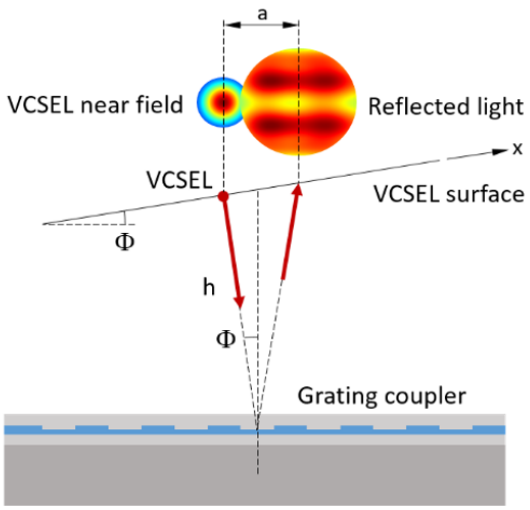

Fig. 8. Optical feedback caused by specular reflection at the GC. The VCSEL-to-GC distance h depends on D and Φ via h = D·tan(Φ). The distance a between the VCSEL and the center of the reflected light also depends on D and Φ.

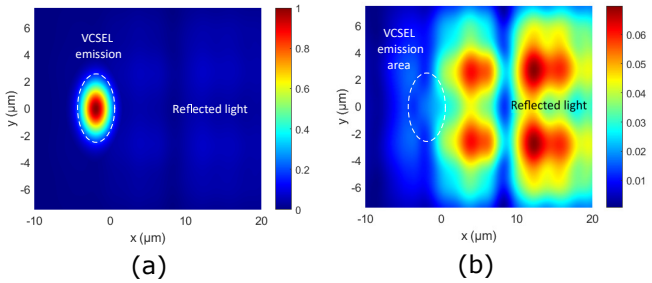

Fig. 9. Electrical field amplitudes at the VCSEL surface with D = 150 μm and Φ = 11° for the contra-directional coupling case, with grating period for maximum coupling efficiency. (a) 3D simulations, both VCSEL near-field and reflected light. (b) 3D simulations, reflected light only.

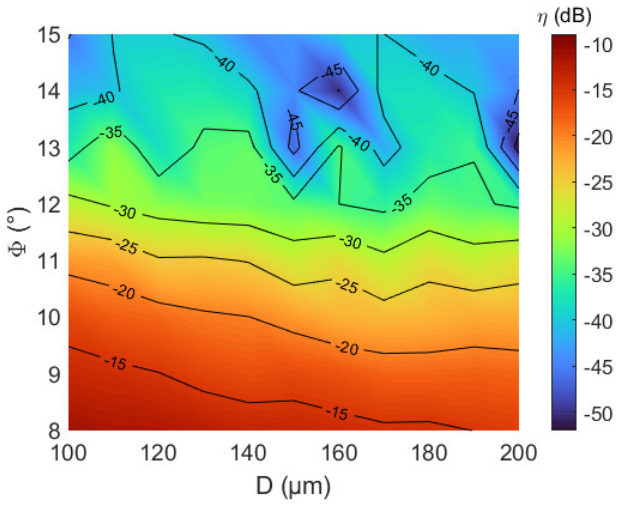

(a) Contra-directional coupling

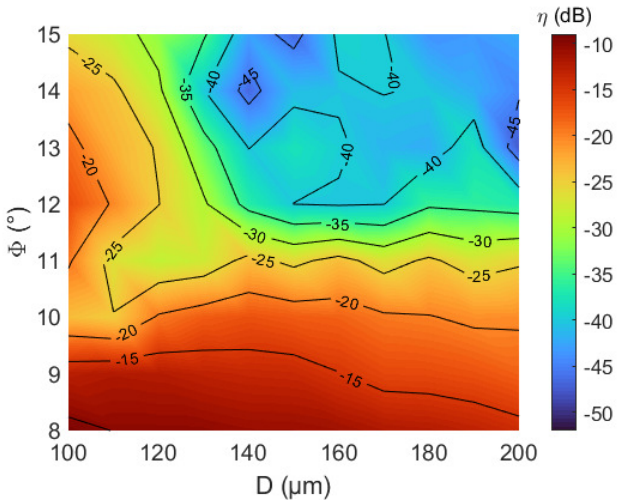

(b) Co-directional coupling

Fig. 10. Optical feedback with contra-directional (a) and co-directional (b) coupling.

of the VCSEL die (Fig. 1). These parameters determine the separation between the VCSEL and the reflected light on the VCSEL surface (distance a in Fig. 8). Increasing angle Φ and length D will increase the separation, thus reducing feedback.

The reflected electric field on the VCSEL was first simulated using 2D FDTD with a linear power monitor placed at the VCSEL surface to capture the reflected light. Fig. 9 shows the amplitudes of the VCSEL near-field and the reflected light from 3D simulations on the surface of the VCSEL with D = 150 μm and Φ = 11° for contra-directional coupling. It is seen that most of the reflected light is at a distance of about 14 μm from the VCSEL in this case, which implies low optical feedback. The reflected beam in Fig. 9(b) is multi-lobed due to interference from multiple reflections from top-cladding, grating layer and the substrate. The simulated 2D optical feedback is -27.4 dB, while the corresponding value from 3D simulations is -27.7 dB. By comparing results from 2D and 3D simulations for several combinations of D and Φ, it was found that the 2D simulations in most cases overestimate the feedback, sometimes by a few dB.

As for the coupling efficiency, optical feedback was calculated for each length D and angle Φ and corresponding grating period for both contra- and co-directional coupling. The results from 2D FDTD simulations are shown in Fig. 10. For both contra- and co-directional coupling, an angle above ~12° is needed to bring the feedback below -30 dB at D = 150 μm. For co-directional coupling, this is close to the critical angle for first-order diffraction loss (13°). Similar to the coupling efficiency, we find that feedback has stronger dependence on Φ than D, for both co- and contra-directional case. The discontinuities in the figure is likely due to the limited resolution (11 steps in D and 8 in angle Φ). The GC design used in this simulation study was conventional for simplicity, but the experiments reported in section 4 allowed for a double-etched staircase design as input GC to further reduce insertion losses.

IV. On-PIC VCSEL-to-fiber and VCSEL-to-photodetector optical links

VCSELs and PDs were flip-chip integrated on a SiN-PIC fabricated on the imec BioPIX300 platform [16]. A schematic

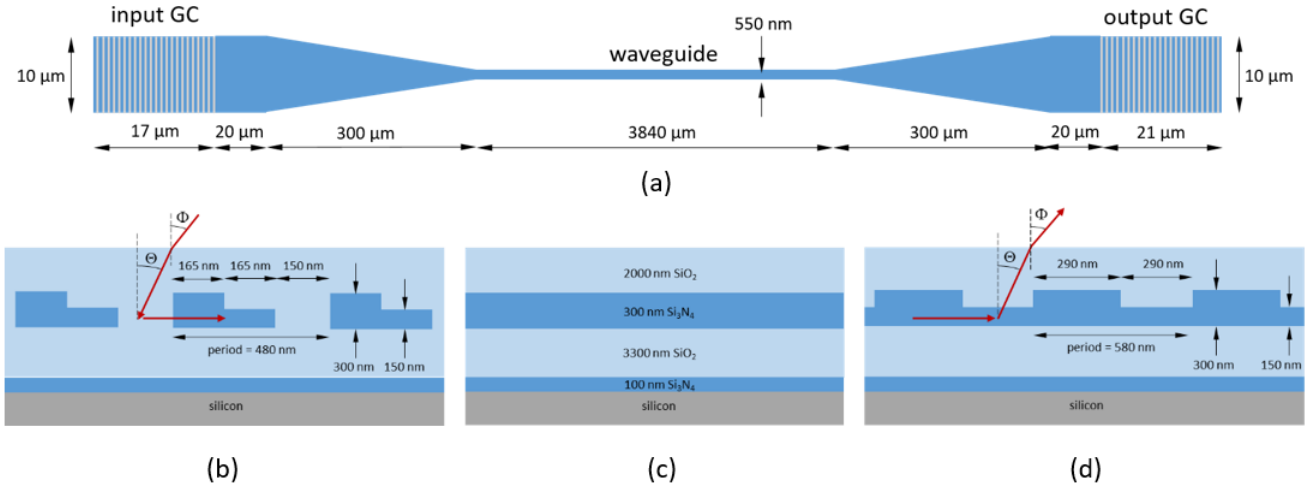

Fig. 11. (a) PIC top view showing the input and output GCs, the SM waveguide, and the tapered waveguide sections connecting the GCs to the SM waveguide. Cross-sections of the input GC (contra-directional), the SM waveguide, and the output GC (co-directional) along the propagation direction are shown in (b), (c), and (d), respectively.

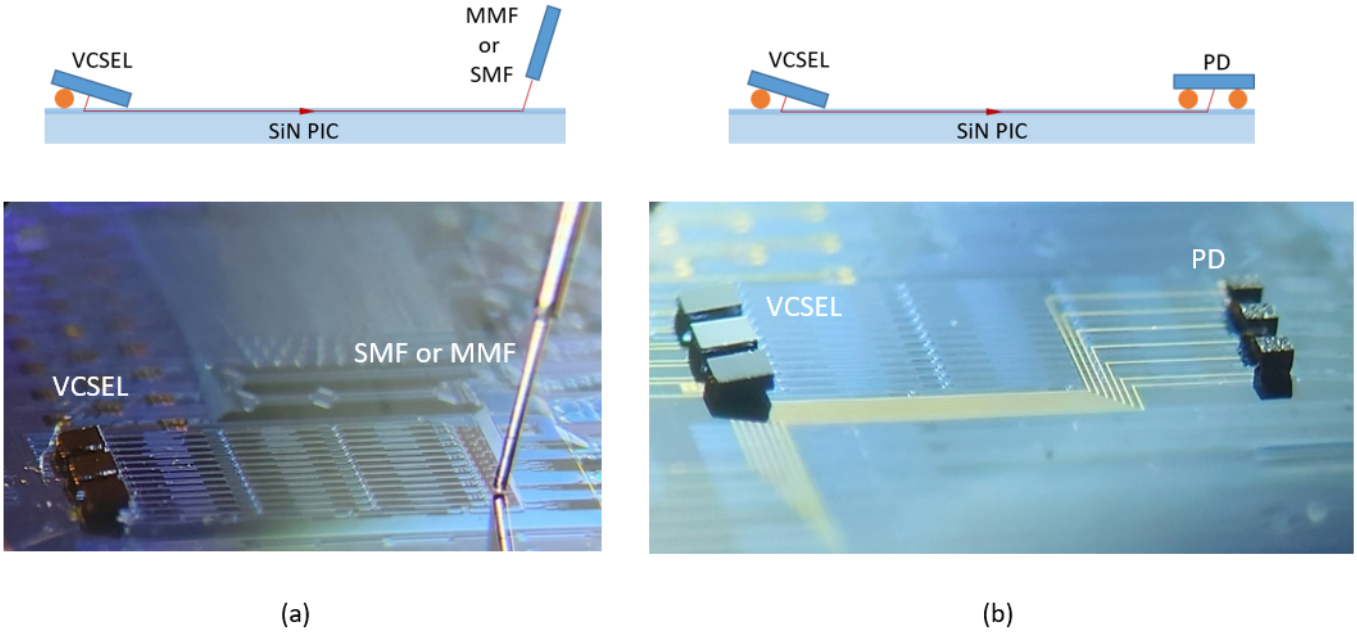

Fig. 12. Illustration (top) and microscope image (bottom) of the VCSEL-to-SMF/MMF (a) and VCSEL-to-PD (b) optical links. The difference in VCSEL angle between the illustrations and images is due to the light from the VCSEL being coupled to the waveguide in the left direction (contra-directional) and the waveguide making an 180° loop-back bend towards the PD where the coupling is co-directional.

of the PIC design is shown in Fig. 11. The core Si_3N_4 layer is 300 nm thick, with a 3.3 µm thick lower SiO_2 cladding and a 2.0 µm thick upper SiO_2 cladding (same as in the FDTD analysis in Section 3). Between the Si substrate and the lower SiO_2 cladding layer there is a 100 nm thick Si_3N_4 anti-reflection layer (the thickness of the lower SiO_2 cladding then has no impact on the device performance). Input and output GCs are connected using a 3840 µm long SM waveguide with a 550 nm wide Si_3N_4 core. 300 µm long tapered waveguide sections are used to adiabatically connect the GCs to the SM waveguide.

The input (output) GC is 17 (20) µm long and 10 µm wide with constant grating period (non-apodized) and straight grating lines. The gratings were etched into the Si_3N_4 core before deposition and chemo-mechanical polishing of the top SiO_2 cladding layer. The input GC has a dual-etch (150 and 300 nm) staircase grating with a period of 480 nm for contra-directional coupling while the output GC has a single-etch (150 nm) grating with a period of 580 nm for co-directional coupling. The GCs are designed for in- and out-coupling angles of ~11° at the wavelength of 850 nm.

Optimizations in 2D FDTD were made to maximize the

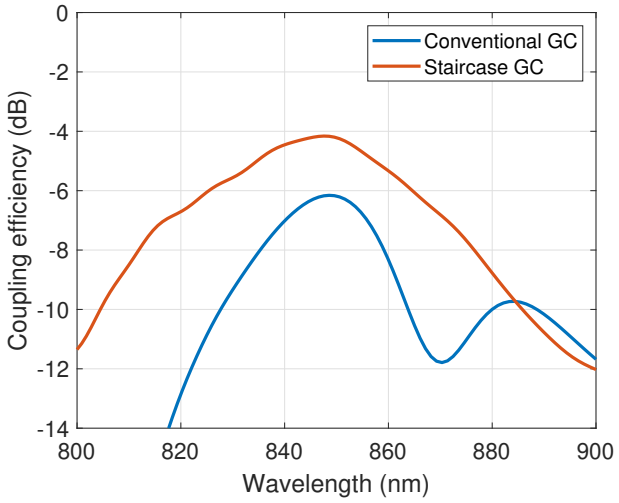

Fig. 13. 2D FDTD simulations of coupling efficiency of a conventional GC and of a staircase GC with D = 145 µm and Φ = 11° for the contra-directional case both with grating period for maximum coupling efficiency. The conventional and staircase GC have a period of respectively 465 nm and 480 nm.

coupling efficiency of the staircase grating. The simulations were carried out to compare the device performance with the conventional GC in the previous sections in the case D = 145 µm and Φ = 11°. The duty cycle for the staircase GC was optimized to 69%. The results are shown in Fig. 13. We see that the staircase GC outperforms the conventional GC by approximately 2 dB. Moreover, the staircase design has a larger 3 dB bandwidth: 55 nm vs. 30 nm for the conventional GC. Finally, the simulated optical feedback are similar in the two cases: -24.55 dB for the staircase design and -25.22 dB for the conventional design.

The insertion loss of the optical channel (input GC - waveguide - output GC) and the coupling loss of the GCs were first measured using optical fibers at an angle of 11° and a distance < 25 µm at the input and output GCs. A singlemode fiber (SMF), together with a tunable laser tuned to 850 nm, was used at the input GC together with a polarization controller to align the polarization of the incident light parallel to the grating lines. The SMF (Thorlabs 70 HP) has a core diameter of 4.4 µm, a mode field $1/e^2$ diameter of 5.0 µm and a numerical aperture of 0.13. The beam delivered by the SMF has a $1/e^2$ full divergence angle of 12°. At the output GC, either the same SMF or a multimode fiber (MMF, OZ Optics MMF-IRVIS-62.5/125-3-L) with a 62.5 µm graded index core and a numerical aperture of 0.275 was used. With the SMF at the output GC (SMF-to-SMF), we measured an insertion loss of 18.5 dB. This is divided between 9.0 dB input coupling loss, 0.3 dB waveguide loss, and 9.2 dB output coupling loss. The loss of the output GC was determined by a measurement on a channel with the input GC being identical to the output GC and assuming equal input and output GC loss. With the MMF at the output (SMF-to-MMF), the output coupling loss was reduced by ~4 dB due to the higher coupling efficiency to the MMF. This yields an insertion loss of -14.5 dB. These numbers are used as a reference for VCSEL-to-SMF, VCSEL-to-MMF, and VCSEL-to-PD insertion loss measurements.

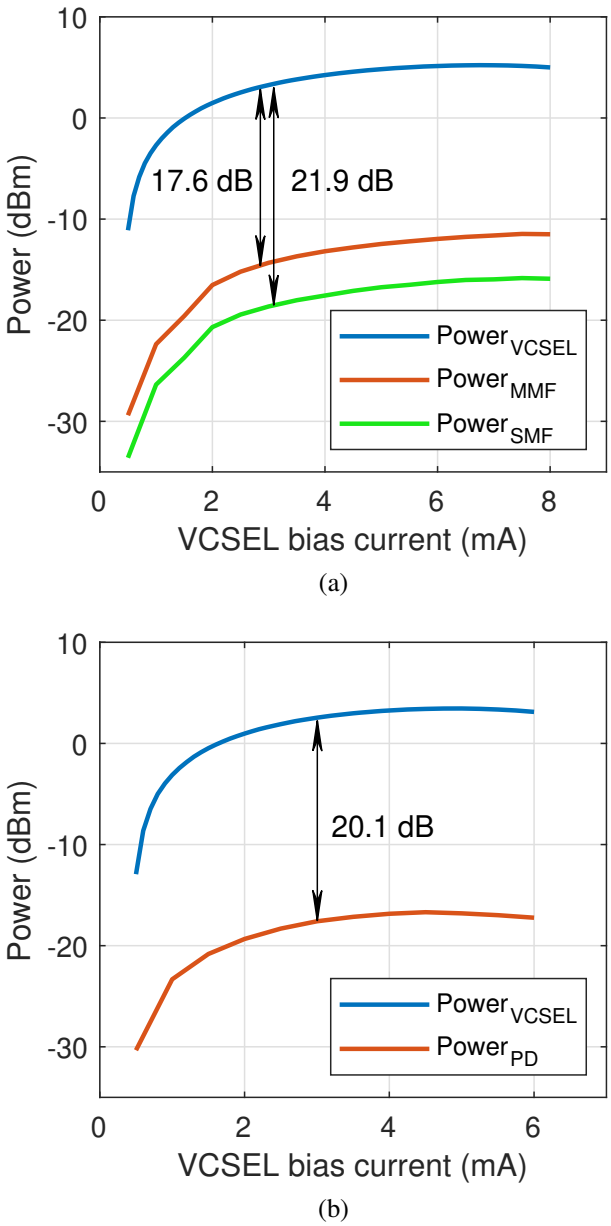

Fig. 14. (a) Detected optical power vs. VCSEL bias current with SMF (green) and MMF (red) at the output GC. (b) Detected optical power vs. VCSEL bias current with the PD at the output GC (red). In both graphs, the measured VCSEL output power before flip-chip integration is shown by the blue curve.

The VCSELs used for angled flip-chip integration over the input GCs are GaAs-based oxide-confined 850 nm SM-VCSELs with a transverse and polarization mode filter etched into the surface of the VCSEL [13]. Suppression of higher order transverse modes and the orthogonal polarization state exceeds 30 and 20 dB, respectively. The direction of polarization is controlled such that the light is polarized parallel to the grating lines of the input GC after flip-chip integration. The beam produced by the VCSEL is near Gaussian with a $1/e^2$ waist diameter of 3.8 µm and a $1/e^2$ full divergence angle of 16° (same as in the FDTD analysis in Section 3). The divergence is somewhat larger than that of the beam delivered

by the SMF (12°). The distance from the VCSEL to the edge of the VCSEL die (distance D in Fig. 1) is 145 µm. The PDs flip-chipped over the output GCs are GaAs-based PDs from VI Systems (D20-850C) with a 20 µm diameter optical aperture and a responsivity of 0.4 A/W at 850 nm.

The VCSEL flip-chip integration process starts with the application of 40 µm diameter AuPd stud bumps on the metal pads on the PIC using a ball wire bonder, coined flat to a thickness of 20 µm. This is followed by deposition of 50 µm diameter SnAgCu solder balls for a total height of 70 µm before flip chipping. Flip-chip integration was done using a Finetech Lambda manual flip-chip bonder with a lateral placement accuracy of ±0.5 µm and an angle accuracy of ±2°. The target height of the stud bump + solder ball after flip chipping is 38 µm for an angle of 11°. A similar process was used for flip-chip integration of the PDs, but the PDs are horizontal (angle = 0°). Fig. 12 shows illustrations and microscope images of the VCSEL-to-SMF/MMF and VCSEL-to-PD optical links.

Results from VCSEL-to-SMF and VCSEL-to-MMF measurements are shown in Fig. 14(a). The insertion loss, defined as the ratio of the power collected by the fiber to the total output power in free space of the VCSEL, is 21.9 dB for the VCSEL-to-SMF link and 17.6 dB for the VCSEL-to-MMF link. The loss difference of 4.3 dB, due to the higher coupling efficiency to the MMF, is consistent with the SMF-to-SMF and SMF-to-MMF measurements. The insertion loss when using a VCSEL at the input GC is about 3 dB higher than when using an SMF, for both SMF and MMF at the output GC. This comes partly from the placement and angle accuracy of the flip-chip integration process and partly from the beam from the VCSEL being somewhat more divergent than the beam from the SMF.

Results from VCSEL-to-PD measurements are shown in Fig. 14(b). The insertion loss is 20.1 dB. This is about 1.8 dB smaller than for the VCSEL-to-SMF link and about 2.5 dB higher than for the VCSEL-to-MMF link, which reflects the difference in coupling efficiency from the output GC to the SMF, MMF, and PD. The PD had an aperture of 20 µm of diameter while the MMF had a 62.5 µm core diameter, which could explain the higher coupling loss to the PD than to the MMF.

For a comparison, the measured insertion loss for all cases (SMF and VCSEL at input GC and SMF, MMF, and PD at output GC) are shown in Fig. 15. In the cases with a SM-VCSEL at the input GC, no feedback-induced instabilities were observed in either the light-voltage-current or spectral characteristics of the VCSEL. Therefore, the angle and VCSEL-to-GC distance are large enough to avoid such instabilities.

The GC coupling efficiencies deduced from the fiber-to-fiber measurements are relatively low at about -9 dB for the input GCs (SMF) and about -5 and -9 dB for the output GCs (MMF and SMF). This is due to 1) the low refractive index contrast between Si_3N_4 and SiO_2 [1], 2) the small GC area which for the input GC may lead to some of the light from the SMF illuminating areas outside the GC, and 3) the GC designs not being optimized. For instance, with an apodized grating with curved grating lines for improved mode matching [6] and/or a distributed Bragg reflector below the waveguide for re-directing light transmitted through the GC, the efficiency can be improved to ~ -2 dB with a sufficiently large grating area [17].

As stated earlier, the ~3 dB higher insertion loss when using a VCSEL at the input GC, compared to using an SMF, comes partly from non-identical beams delivered by the VCSEL and the SMF and partly from the placement and angle accuracy of the flip-chip integration process. The larger divergence of the VCSEL beam means that more light is illuminating areas outside the GC. To study the impact of the ±2° angle accuracy, which translates to a ±5 µm variation of VCSEL-to-GC distance when D = 145 µm, we used 3D FDTD to simulate the dependence of coupling efficiency on angle (from 9° to 13°) and wavelength for the input dual-etch staircase GC shown in Fig. 11(b). The spot position on the input GC was adjusted for highest coupling efficiency. The results in Fig. 16(a) reveal a ~1 dB variation of coupling efficiency at 850 nm. However, as the angle deviates from the optimum, also the light spot position on the GC moves from the optimum position by about ±1 µm. This adds to the placement accuracy of ±0.5 µm. Fig. 16(b) shows the simulated (3D) dependence of coupling efficiency on spot position along the coupling direction when the angle is 11°. A ±2 µm deviation from the optimum spot position in the coupling direction (x-direction) results in a reduction of coupling efficiency by ~1.5 dB. In the perpendicular direction (y-direction), the coupling efficiency is reduced by 0.3 dB with the same deviation. We conclude that deviations from optimum angle and optimum spot position alone can add up to several dB of variation of the coupling efficiency. Therefore, high accuracy in VCSEL placement and angle is needed for a high and reproducible coupling efficiency.

We finally note that the coupling efficiency under optimum angle and position predicted by the 3D simulations (~-5 dB, Fig. 16) is higher than measured with the aligned SMF (~-9 dB) and the flip-chip integrated VCSEL (~-12 dB). While the

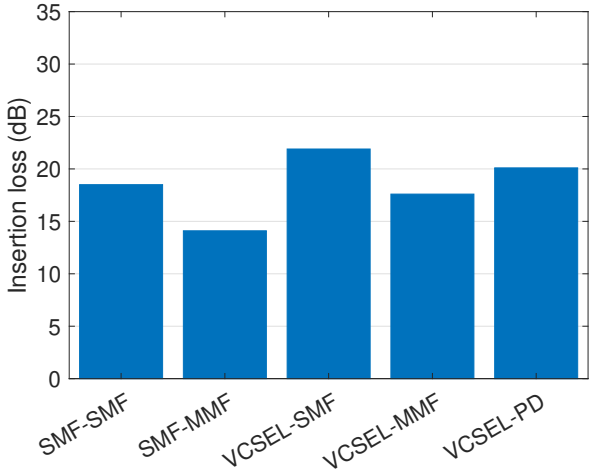

Fig. 15. Comparison of insertion loss of all channels with SMF or VCSEL at the input GC and SMF, MMF or PD at the output GC.

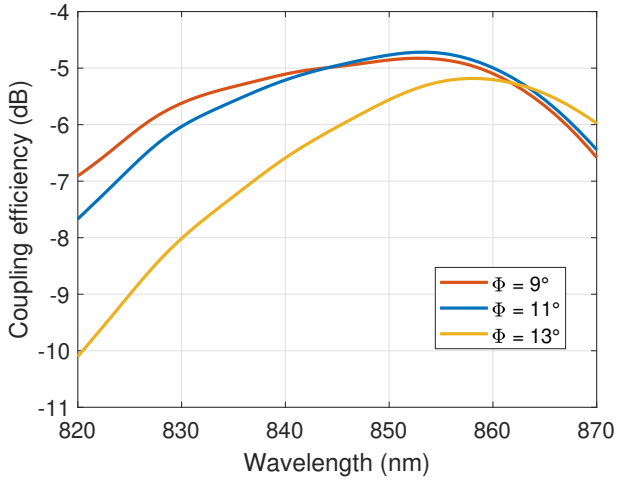

(a)

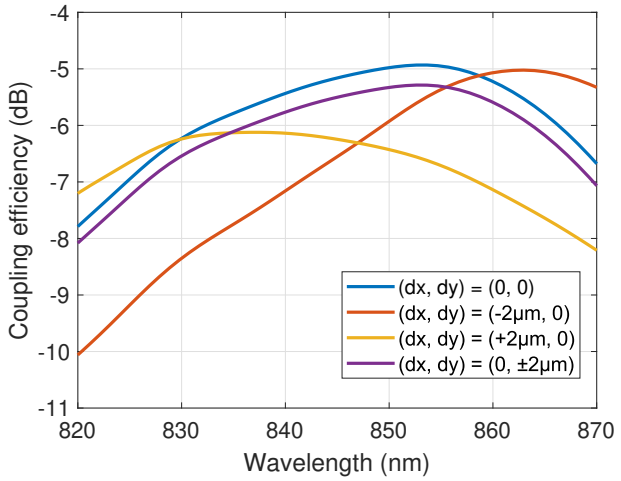

(b)

Fig. 16. Simulations of coupling efficiency with D = 145 μm, Φ = 11° for the contra-directional case when (a) Φ deviates by ±2° and when (b) the spot on the GC deviates by ±2 μm in the x- or y-direction from its optimal position. dx and dy denote the deviation of the spot on the GC from its optimal position. The grating period is 485 nm and the blue curves correspond to the case when Φ = 11° with the spot in its optimal position on the GC.

difference between the VCSEL and SMF coupling efficiency can be explained by the flip-chip angle and placement accuracy, the difference between the measured SMF and simulated coupling efficiency remains to be examined. We also noticed 2.4 dB coupling difference between two different mounted VCSEL samples for contra-directional case. The input and output GCs were designed in the same way as shown in Fig. 11. The first VCSEL was flip-chipped at an angle of 11.6° and the other at 10.5°, which represented a difference of 1.1° between the two samples (the target angle was 11°). An output MMF was used to measure the insertion loss for the first VCSEL and a PD was used for the second. The resulting coupling losses were 19.1 dB and 21.5 dB respectively. The other channels available with mounted VCSELs used different GC designs, so they could not be used for an apples-to-apples comparison.

Fig. 17 shows the measured spectral emission characteristics

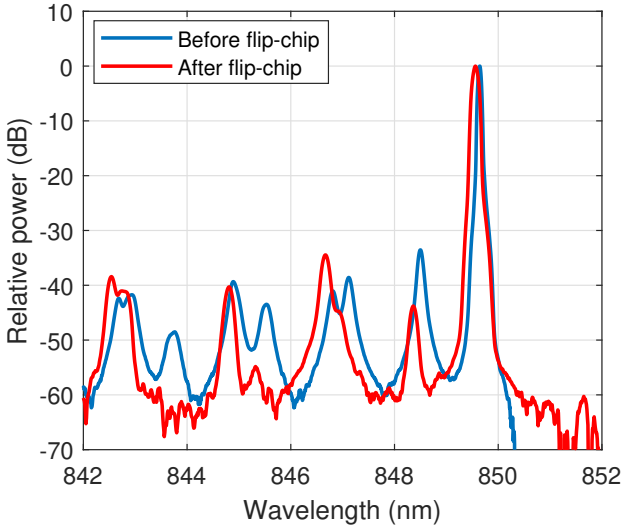

Fig. 17. SM-VCSEL spectra before and after mounting on the PIC at 3 mA and 25°C.

of the VCSEL before flip-chip mount (by aligning a fiber to the output facet of the VCSEL) and after flip-chip mount (by aligning a fiber to the output GC). The spectra are very similar and show that the VCSEL remains singlemode with a higher order mode suppression of more than 30 dB.

V. Summary and Conclusions

We have investigated the dependence of coupling efficiency and optical feedback for a linearly polarized SM-VCSEL flip-chip integrated at an angle over a GC on angle and VCSEL-to-GC distance using 2D and 3D FDTD simulations. Both show a relatively strong dependence on angle and a weaker dependence on distance. With both coupling efficiency and feedback being reduced with increasing angle, there is a trade-off. For co-directional coupling, light is diffracted into the cladding layers of the waveguide beyond a critical angle. If an angle beyond the critical angle is needed for sufficiently low feedback, a coupling efficiency penalty occurs. For contra-directional coupling, diffraction into the cladding layers cannot occur at any angle. This is therefore the preferred coupling scheme.

A specific case was studied: an 850 nm SM-VCSEL flip-chip integrated over a GC on a Si_3N_4/SiO_2-on-Si PIC with a certain grating design and GC dimension. However, the results are generic in terms of the dependence of coupling efficiency and optical feedback on angle and distance and the appearance of additional diffraction loss for co-directional coupling beyond a critical angle. On the other hand, the specific numbers for coupling efficiency, feedback and critical angle depend on VCSEL beam divergence and wavelength, waveguide and grating parameters, as well as GC design and dimensions.

In the second part, we experimentally demonstrate on-PIC VCSEL-to-SMF/MMF and VCSEL-to-PD optical links using 850 nm SM-VCSELs flip-chip integrated on the same Si_3N_4/SiO_2-on-Si PIC platform used in the simulations. The

difference in measured insertion loss correlates with the expected difference in coupling efficiency between the output GC and SMF, MMF or PD. A few dB higher insertion loss was observed when using a VCSEL at the input GC compared to a well-aligned SMF. This comes partly from the larger beam divergence of the VCSEL and partly from misalignments during flip-chip integration. We therefore also conducted a numerical analysis of the sensitivity of the coupling efficiency to various misalignment parameters. We found that, within the tolerances of the flip-chip integration process, there is a few dBs of variation of the coupling efficiency.

ACKNOWLEDGMENT

This work was funded by European Union's Horizon 2020 research and innovation program (688519, PIX4life) and the Swedish Research Council (2016-06077, iTRAN).

REFERENCES

[1] Z. Wang, A. Abbasi, U. Dave, A. D. Groote, S. Kumari, B. Kunert, C. Merckling, M. Pantouvaki, Y. Shi, B. Tian, K. V. Gasse, J. Verbist, R. Wang, W. Xie, J. Zhang, Y. Zhu, J. Bauwelinck, X. Yin, Z. Hens, J. V. Campenhout, B. Kuyken, R. Baets, G. Morthier, D. V. Thourhout, and G. Roelkens, "Novel light source integration approaches for silicon photonics," *Laser Photonics Reviews*, vol. 11, no. 4, 2017.

[2] H. Lu, J. S. Lee, Y. Zhao, C. Scarcella, P. Cardile, A. Daly, M. Ortsiefer, L. Carroll, and P. O'Brien, "Flip-chip integration of tilted VCSELs onto a silicon photonic integrated circuit," *Optics Express*, vol. 24, no. 15, pp. 16 258–16 266, 2016.

[3] J. Zhang, G. Muliuk, J. Juvert, S. Kumari, J. Goyvaerts, B. Haq, C. O. D. Beeck, B. Kuyken, G. Morthier, D. V. Thourhout, R. Baets, G. Lepage, P. Verheyen, J. V. Campenhout, A. Gocalinska, J. O'Callaghan, E. Pelucchi, K. Thomas, B. Corbett, A. Trindade, and G. Roelkens, "III-V-on-Si photonic integrated circuits realized using micro-transfer-printing," *APL Photonics*, vol. 4, 2019.

[4] R. Marchetti, C. Lacava, L. Carroll, K. Gradkowski, and P. Minzioni, "Coupling strategies for silicon photonics integrated chips," *Photonics Research*, vol. 7, no. 2, pp. 201–239, 2019.

[5] T. Pinguet, S. Denton, S. Gloeckner, M. Mack, G. Masini, A. Mekis, S. Pang, M. Peterson, S. Sahni, and P. D. Dobbelaere, "High-volume manufacturing platform for silicon photonics," *Proceeding of IEEE*, vol. 106, no. 12, pp. 2281–2290, 2018.

[6] L. Cheng, S. Mao, Z. Li, Y. Han, and H. Y. Fu, "Grating couplers on silicon photonics: design principles, emerging trends and practical issues," *Micromachines*, vol. 11, no. 666, 2020.

[7] X. Hu, M. Girardi, Z. Ye, P. Munoz, A. Larsson, and V. Torres-Company, "Passive Si_3N_4 photonic integration platform at 1 μm for short-range optical interconnects," *Optics Express*, vol. 28, no. 9, pp. 13 019–13 031, 2020.

[8] A. Hänsel and M. J. R. Heck, "Opportunities for photonic integrated circuits in optical gas sensors," *J. Phys. Photonics*, vol. 2, no. 1, 2020.

[9] Y. Wang, S. Djordjevic, J. Yao, J. Cunningham, X. Zheng, A. Krishnamoorthy, M. Muller, M. Amann, R. Bojko, N.A.F, Jaeger, and L. Chrostowski, "Vertical-cavity surface-emitting laser flip-chip bonding to silicon photonics chip," 2015.

[10] K. Kaur, A. Subramanian, P. Cardile, R. Verplancke, J. V. Kerrebrouck, S. Spiga, R. Meyer, J. Bauwelinck, R. Baets, and G. V. Steenberge, "Flip-chip assembly of VCSELs on silicon gratings couplers via laser fabricated SU8 prisms," *Optics Express*, vol. 23, no. 22, pp. 28 264–28 270, 2015.

[11] Z. Ruan, Y. Zhu, P. Chen, Y. Shi, X. Cai, and L. Liu, "Efficient hybrid integration of long-wavelength VCSELs on silicon photonic circuits," *IEEE Journal of Lightwave Technology*, vol. 38, no. 18, pp. 5100–5106, 2020.

[12] J. Y. Law and G. P. Agrawal, "Effects of optical feedback on static and dynamic characteristics of vertical-cavity surface-emitting lasers," *IEEE Sel. Top. Quantum Electron*, pp. 353–358, 1994.

[13] E. Haglund, M. Jahed, J. S. Gustavsson, A. Larsson, J. Goyvaerts, R. Baets, G. Roelkens, M. Rensing, and P. O'Brien, "High-power single transverse and polarization mode VCSEL for silicon photonics integration," *Optics Express*, vol. 27, no. 13, pp. 18 892–18 899, 2019.

[14] *www.lumerical.com*.

[15] S. Nambiar, P. Ranganath, R. Kallega, and S. K. Selvaraja, "High efficiency DBR assisted grating chirp generators for silicon nitride fiber-chip coupling," *Scientific Reports*, vol. 9, no. 18821, 2019.

[16] *https://europractice-ic.com/mpw-prototyping/siphotonics/imec/*.

[17] H. Zhang, C. Li, X. Tu, J. Song, H. Zhou, X. Luo, Y. Huang, M. Yu, and G. Lu, "Efficient silicon nitride grating coupler with distributed Bragg reflector," *Optics Express*, vol. 22, no. 18, pp. 21 800–21 805, 2014.